

VoroUDF: Meshing Unsigned Distance Fields with Voronoi Optimization

NINGNA WANG, Columbia University, USA
 ZILONG WANG, University of Texas at Dallas, USA
 XIANA CARRERA, Columbia University, USA
 XIAOHU GUO, University of Texas at Dallas, USA
 SILVIA SELLÁN, Columbia University, USA



Fig. 1. We propose an algorithm for reconstructing surfaces with non-manifold structures (highlighted in red), sharp features, and open boundaries from unsigned distance fields with gradient information.

We present VoroUDF, an algorithm for reconstructing high-quality triangle meshes from Unsigned Distance Fields (UDFs). Our algorithm supports non-manifold geometry, sharp features, and open boundaries, without relying on error-prone inside/outside estimation, restrictive look-up tables nor topologically noisy optimization. Our Voronoi-based formulation combines a L_1 tangent minimization with feature-aware repulsion to robustly recover complex surface topology. It achieves significantly improved topological consistency and geometric fidelity compared to existing methods, while producing lightweight meshes suitable for downstream real-time and interactive applications.

1 Introduction

Unsigned Distance Fields (UDFs) have emerged as a powerful representation for shapes of arbitrary topology containing sharp and even non-manifold features. Their ability to represent thin, geometrically challenging self-intersecting structures has made them popular in artistic 3D modeling applications (see Figure 1), while their flexibility has increased their adoption in learning-based shape representations and reconstruction pipelines for real-world geometry. Reconstructing high-quality surface meshes with non-manifold structures, open boundaries, and sharp features from UDFs is critical for downstream applications such as texture mapping, physical simulation, animation, and geometric processing.

However, converting a UDF into an explicit surface mesh remains challenging. Without a consistent sign to differentiate inside from outside, classic grid-based iso-surfacing techniques [Ju et al. 2002; Lorensen and Cline 1987] cannot be directly applied. Methods that

combine sign estimation with Marching Cubes lookup tables [Guillard et al. 2022; Ren et al. 2023; Stella et al. 2024; Zhou et al. 2022] are highly unstable around thin regions and fail to reconstruct non-manifold structures (see Figure 1, second and third from left). Dual grid contouring approaches with purpose-made quadratic optimizations [Zhang et al. 2023] produce topological noise and undesirable non-manifold edges missing from the input (Figure 1, second from right). When non-manifold features are intentionally present in the input (e.g., Figure 1, left), algorithms based on contracting a surface mesh of a volumetric offset [Chen et al. 2025; Hou et al. 2023] cannot recover them by design (Figure 1, third from right).

In this paper, we introduce a Voronoi-based optimization framework for extracting isosurfaces with non-manifold structures, open boundaries, and sharp features from UDFs. In contrast to recent grid-based methods that rely on fixed spatial partitions, our Voronoi-based decomposition adapts to the distribution of discrete seeds in space, enabling a more flexible and geometry-aware partitioning. We iteratively solve a local L_1 tangent energy minimization and a global seed distribution problem to optimize seed positions such that they automatically align with complex surface features. Connectivity is directly derived from the Voronoi adjacency, resulting in cleaner and more topologically consistent meshes than those produced by grid-based methods (Figure 1, right).

Through extensive qualitative and quantitative evaluations on synthetic non-manifold shapes and real-world datasets [Koch et al. 2019; Zhu et al. 2020], we demonstrate that our method outperforms prior work in reconstructing non-manifold structures, open boundaries, and sharp features. Our algorithm will be most impactful in artistic and industrial design contexts, as it is able to recover the geometrically challenging, topologically degenerate shapes common in these. Critically, it does so without resorting to an excessively dense discretization, producing lightweight meshes that are directly portable to real-time and interactive applications.

Authors' Contact Information: Ningna Wang, Columbia University, New York, USA, ningnalala@gmail.com; Zilong Wang, University of Texas at Dallas, Richardson, USA, Zilong.Wang@utdallas.edu; Xiana Carrera, Columbia University, New York, USA, xiana.carrera.alonso@gmail.com; Xiaohu Guo, University of Texas at Dallas, Richardson, USA, xguo@utdallas.edu; Silvia Sellán, Columbia University, New York, USA, sgs2195@columbia.edu.

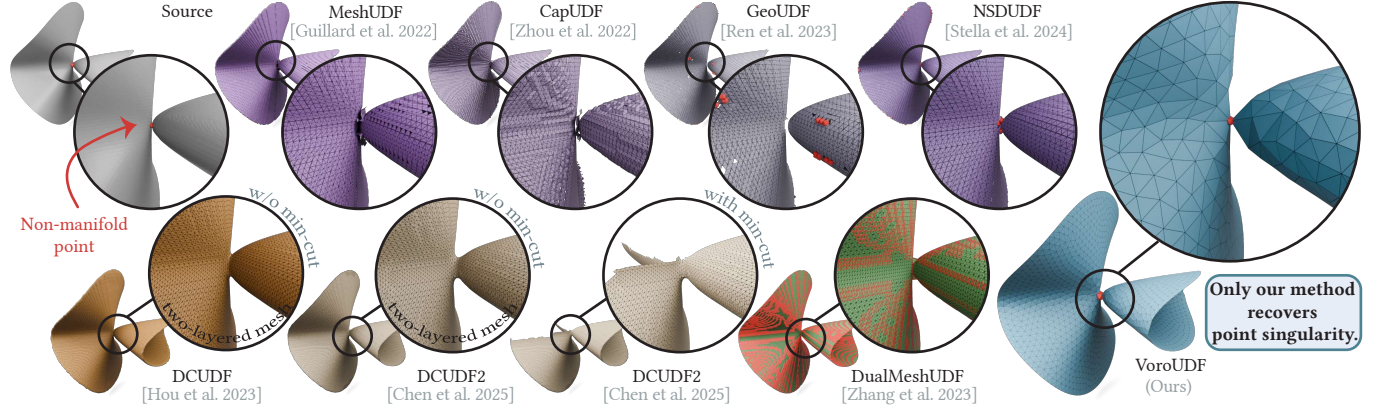


Fig. 2. Unlike marching-cube-based methods [Guillard et al. 2022; Ren et al. 2023; Stella et al. 2024; Zhou et al. 2022] that rely on pseudo-sign estimation, double-covering-based methods [Chen et al. 2025; Hou et al. 2023] that produce double-layered meshes, and dual-contouring-based methods [Zhang et al. 2023] that introduce erroneous connectivity, our method is the only approach capable of reconstructing non-manifold structures (highlighted in red).

2 Related Work

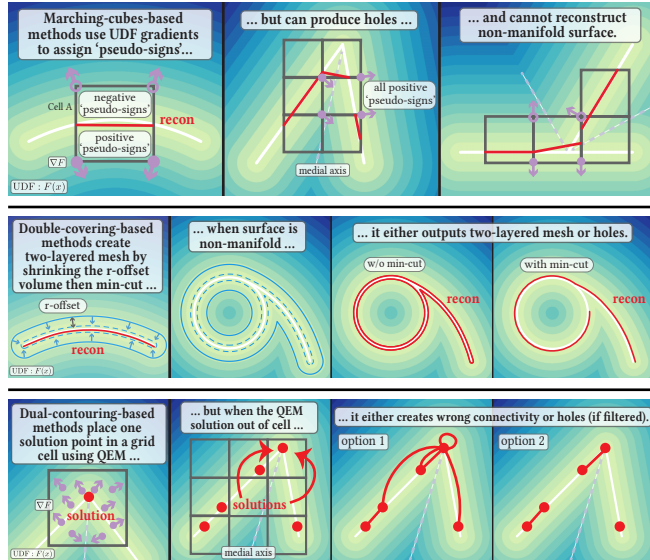


Fig. 3. Illustration of why marching-cubes-based methods (top row), double-covering-based methods (middle row), and dual-contouring-based methods (bottom row) fail to preserve the non-manifoldness of the iso-surface.

UDFs can represent surfaces of arbitrary topology, making them particularly valuable in domains such as artistic modeling, manufacturing, and industrial design, where accurate recovery of complex surface structures is critical. Owing to this flexibility, UDFs have become a powerful tool across a wide range of scientific fields—from medical imaging [Jin et al. 2024; Sørensen et al. 2022] to geology [Zhang et al. 2026] and additive manufacturing [Brunton and Rmaileh 2021]. In computer graphics, their expressive capacity has been extensively utilized in geometric deep learning and generative 3D modeling [Chibane et al. 2020; Liu et al. 2023; Long et al. 2023; Xu et al. 2025; Zhao et al. 2021].

Despite their expressiveness, UDFs remain poorly suited for many downstream applications due to its implicit nature. Tasks such as finite element simulation, texture mapping, real-time rendering, and animation often require converting UDFs into explicit surface representations like polygonal meshes. This conversion is nontrivial: UDFs lack orientation and sign information, making direct mesh extraction challenging. As a result, robust UDF-to-mesh reconstruction remains a central problem in geometry processing. Several recent strategies have been explored to reconstruct a surface mesh from a UDF, each with important limitations.

Marching-cubes-based methods. One family of methods adapts grid-based isosurface extraction (e.g., Marching Cubes variants) to UDFs by introducing a pseudo-sign per grid cell [Guillard et al. 2022; Ren et al. 2023; Zhou et al. 2022]. These approaches attempt to infer on which side of the surface each voxel corner lies (since all UDF values are positive) by analyzing the UDF’s gradients or other heuristics. Essentially, they locally treat the UDF as a signed field and then apply the Marching Cubes lookup to extract a mesh. This works only under a key assumption: each grid cell that contains the surface must lie entirely on one side of the surface’s medial axis. If a cell spans across the medial axis, the pseudo-sign becomes ill-defined and unstable (see Fig. 3 top row). The learning-based method NSDUDF [Stella et al. 2024] predicts pseudo-sign information from local views, however, it struggles to generalize and may fail to produce accurate results on previously unseen shapes or topologies, particularly in regions with non-manifold geometry.

Double-covering-based methods. Another approach is to temporarily convert the open or non-manifold surface into a closed manifold by using a double covering technique [Chen et al. 2025; Hou et al. 2023]. This approach extracts a thin offset surface around the target shape, which forms a closed, orientable manifold, and then optimizes this double-layered surface onto the direction of isosurfaces. This yields a valid mesh even when the input surface is open. If the input surface is truly non-manifold, however, the method cannot

produce a single unified mesh, as it instead retains two overlapping surface layers at the non-manifold regions (see Fig. 3 middle row).

Dual-contouring-based methods. To avoid relying on a global pseudo-sign, researchers have also proposed dual-contouring-based methods for UDF meshing. The learning-based method NDC [Chen et al. 2022] enhances the classic Dual Contouring algorithm by refining UDFs using learned priors; however, it struggles to generalize to shapes with arbitrary topology and unseen geometric configurations. A recent example is DualMeshUDF [Zhang et al. 2023], which uses an adaptive octree and computes each mesh vertex by solving a quadratic error function (QEF) that fits the local unsigned field (analogous to finding the intersection of estimated tangent planes). These approaches can directly place vertices on the surface without requiring sign flips, enabling it to capture sharp edges and even non-manifold structures that Marching Cubes variants might miss. However, ensuring topologically correct connectivity becomes challenging for such dual methods, as they all rely on the assumption that the solution space will not be far from the grid cell and then minimizes towards a point inside of the cell close to the solution. The erroneous connectivity appears when the reconstructed surface point computed for an octree cell lies outside the cell. If these noisy points are discarded or clamped, the mesh quality is compromised by holes (see Figure 3 bottom row). In practice, DualMeshUDF filters out vertices that fall outside their cell, which means those cells end up with no mesh vertex and thereby produce a hole in the reconstructed mesh. This situation tends to occur when a non-empty cell covers surface regions on both sides of its medial axis, causing the QEF solution to drift out of bounds. One might refine the octree further to alleviate this issue, but increasing resolution explosively raises the mesh complexity. For example, in our experiments the Klein bottle model (see Figure 10) required over 13k vertices with DualMeshUDF to avoid holes, whereas a far coarser mesh (roughly 3.6k vertices) suffices with our method. Moreover, DualMeshUDF and similar octree methods impose a maximum depth limit, so they cannot indefinitely subdivide to resolve every ambiguous cell. Hence, some small holes or missed facets may remain if the depth limit is reached.

3 Method

The input to our method is a continuous UDF that provides both unsigned distance values $d = F(\mathbf{x})$ given a point $\mathbf{x} \in \mathcal{R}^3$, which measures proximity to the unknown iso-surface χ , and gradients $\mathbf{n}(\mathbf{x}) = \nabla F(\mathbf{x})/\|\nabla F(\mathbf{x})\|$, which indicate the direction of value increase. In this section, we introduce an iterative optimization algorithm to compute a high-quality triangle mesh $\mathcal{M} = (\mathcal{X}, \mathcal{F})$ that approximates χ while faithfully capturing non-manifold structures, open boundaries, and sharp features.

Unlike grid-based methods that subdivide space using a fixed structure (e.g., an adaptive octree) to locate cells intersecting χ , lacking the flexibility to capture thin structures and often misses features at low resolutions (see Figure 4), our method begins by initializing N movable seeds with gradients $\{\mathbf{x}_i, \mathbf{n}_i\}_{i=1}^N$. These seeds are sampled uniformly within the bounding volume and projected onto the implicit iso-surface χ using their corresponding gradients. We

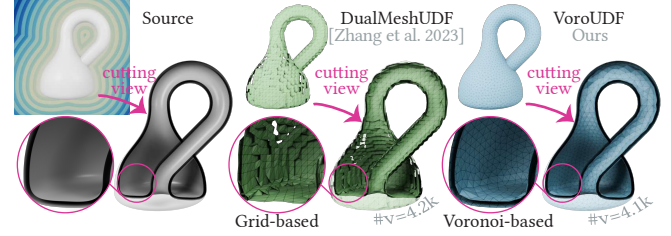


Fig. 4. Dual-contouring-based method [Zhang et al. 2023] uses voxel grids struggles to reconstruct UDF iso-surfaces with thin layers, often resulting in zig-zag connectivity and holes when using a relatively small number of vertices. In contrast, our method, based on a Voronoi partition, avoids these issues and produces clean, consistent connectivity.

then partition the domain into regions via a Voronoi decomposition induced by the seed set $\{\Omega_i\}_{i=1}^N$.

The surface reconstruction is formulated as an iterative optimization of two energy terms: a local tangent energy and a global repulsive energy. The local L_1 tangent energy adjusts the position of each seed \mathbf{x}_i within its corresponding Voronoi cell Ω_i to better fit the local geometry with features. The global repulsive energy redistributes the seeds to improve sampling uniformity on χ and prevent crowding, which enhances numerical stability and triangle quality in the final mesh. After convergence, the output triangle mesh is extracted as the dual of the *geodesic* Voronoi diagram of the optimized seeds. The full algorithm is summarized in Alg. 1.

3.1 L_1 Tangent Energy

We optimize each seed's position \mathbf{x}_i based on the UDF values and gradients of M points $\{\mathbf{p}_{i_m}\}_{m=1}^M$ sampled within its corresponding Voronoi cell Ω_i (we set $M = 100$ in our experiments). Intuitively, the updated seed position should be consistent with the UDF value d_{i_m} and the gradient direction \mathbf{n}_{i_m} at each sample \mathbf{p}_{i_m} . Each sample defines an estimated tangent plane to the iso-surface χ , given by the relation $\mathbf{n}_{i_m}^\top (\mathbf{p}_{i_m} - \mathbf{x}_i) - d_{i_m} = 0$. One may enforce this intuition by minimizing the deviation of the seed \mathbf{x}_i from all such tangent planes using a quadratic energy, as proposed by Zhang et al. [2023] in the context of voxel grids:

$$\mathbf{x}_i^* = \underset{\mathbf{x}_i}{\operatorname{argmin}} \sum_{m=1}^M \left\| \mathbf{n}_{i_m}^\top (\mathbf{p}_{i_m} - \mathbf{x}_i) - d_{i_m} \right\|_2^2. \quad (1)$$

This approach, however, suffers from a longstanding limitation: the optimized point may drift outside its associated cell [Ju et al. 2002; Schaefer and Warren 2002], resulting in invalid connectivity (see Figure 5 (a)). While enforcing hard cell-boundary constraints can prevent this drift, it often pulls the solution away from the actual iso-surface, as illustrated in Figure 5 (b).

To overcome these issues, we introduce a constrained L_1 -norm tangent energy formulated over a Voronoi-based partition. Our L_1 tangent energy for seed \mathbf{x}_i is defined as:

$$E_{tan}(\mathbf{x}_i) = \sum_{m=1}^M \left\| \mathbf{n}_{i_m}^\top (\mathbf{p}_{i_m} - \mathbf{x}_i) - d_{i_m} \right\|_1, \quad (2)$$

summing over all samples in Ω_i . The optimal seed position (approximating the surface point closest to all these tangent planes) is found

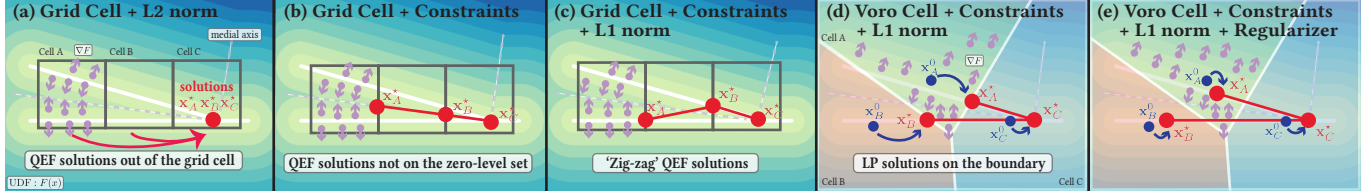


Fig. 5. Illustration of why our formulation uses L_1 tangent energy with Voronoi partitions, rather than L_2 tangent energy with voxel grids.

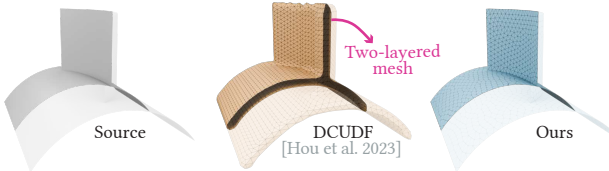


Fig. 6. Our method successfully reconstructs non-manifold structures from UDFs, whereas the double-covering-based method [Hou et al. 2023] returns a two-layered mesh around non-manifold regions.

by minimizing this energy subject to the constraint that \mathbf{x}_i stays within its Voronoi cell boundaries:

$$\min_{\mathbf{x}_i \in \Omega_i} E_{tan}(\mathbf{x}_i) + \gamma \|\mathbf{x}_i - \mathbf{x}_i^0\|_2^2, \quad (3)$$

where the second term in the objective is a proximity regularizer that encourages each seed to remain close to its initial position \mathbf{x}_i^0 , preventing excessive displacement during optimization (we set $\gamma = 10$ in our experiment). Note that minimizing Equation 2 is equivalent to solving the following L_1 linear program:

$$\arg \min_{\mathbf{x}_i} \|A \mathbf{x}_i - b\|_1, \quad (4)$$

where A is a 3×3 matrix and b is a 3×1 vector (3 is the UDF dimension).

This constrained L_1 formulation ensures that \mathbf{x}_i aligns with the local geometry of the zero-level set as inferred from samples within its Voronoi cell, while staying strictly within its designated region. This improves surface fidelity and avoids violations at cell boundaries. Moreover, when Ω_i overlaps a non-manifold or sharp feature, the optimization naturally pulls \mathbf{x}_i onto that feature, ensuring it is accurately preserved in the final mesh.

In contrast, as shown in Figure 6, double-covering-based methods [Chen et al. 2025; Hou et al. 2023] instead return duplicated surface layers around non-manifold regions and cannot recover true connectivity.

3.2 Feature-aware Repulsive Energy

To prevent numerical instability caused by seed crowding and to improve triangle quality in the final mesh, we optimize the spatial distribution of seed positions $\{\mathbf{x}_i\}_{i=1}^N$. This can be achieved using a particle-based repulsion model [Wang et al. 2025; Witkin and Heckbert 1994; Zhong et al. 2013] optimized with L-BFGS. The inter-particle repulsive energy between each pair of distinct seeds (i, j) is defined as:

$$E_{rep} = \sum_i \sum_{j \neq i} E_{rep}^{ij} = \sum_i \sum_{j \neq i} \exp\left(-\frac{\|\mathbf{x}_j - \mathbf{x}_i\|^2}{2\sigma^2}\right), \quad (5)$$



Fig. 7. Our method reconstructs the UDF iso-surface with better triangle quality compared to the marching-cubes-based approach [Ren et al. 2023].

where σ (the *kernel width*) is the standard deviation of the Gaussian kernel. We set σ at each optimization step to the minimum Euclidean distance between any pair of seeds (see Alg. 1, line 4).

However, allowing seeds to move freely within the space without considering geometric features can lead to undesirable effects. For example, seeds may drift completely away from the iso-surface χ during optimization. Inspired by Wang et al. [2025], we introduce a *feature-aware gradient projection strategy* to mitigate this issue using the geometric information extracted from the L_1 tangent energy defined in Sec. 3.1. More specifically, We examine the null space of A in Equation 4 via singular value decomposition (SVD), writing $A = U \Sigma V^T$. If $\text{rank}(A) = r$, then the last $(\dim - r)$ columns of V (denoted V_0) form an orthonormal basis for the null space of A . Our strategy is to project the force $\mathbf{g}^i = \sum_j \nabla E_{rep}^{ij}$ onto this null space:

$$\mathbf{g}_{proj}^i = V_0 V_0^T \mathbf{g}^i, \quad (6)$$

ensuring that the gradient update lies in the feature-preserving subspace. In practice, this restricts movement to feature-consistent directions. For example, a seed that has converged to a non-manifold edge will only be updated along that edge, preserving sharp or singular structures during optimization.

In summary, our method produces high-quality triangle meshes, as shown in Figure 7, due to the repulsive energy formulation combined with feature-aware gradient projection.

3.3 Mesh Reconstruction via the Dual of a Geodesic Voronoi Diagram

After optimizing the seeds, the next step is to connect them to form a triangle mesh. A natural approach is to use the dual of the Voronoi diagram (*i.e.*, the Delaunay triangulation) to establish connectivity among seeds. However, a standard Voronoi diagram computed in the entire domain is unrestricted; it may erroneously connect seeds on different layers of the iso-surface even if they are far apart on the surface. Even a restricted Voronoi diagram can fail in thin-plate scenarios: a single site may dominate multiple surface regions when the iso-surface is a thin plate and the number of seed points is

insufficient. For example Figure 8 (a), the dual of the VD contains extra edge from x_A to x_B as their Voronoi cells are adjacent.

To address these issues, we propose a reconstruction method based on the *Geodesic Voronoi Diagram* (GVD) defined on the iso-surface itself, shown in Figure 8 (b). Instead of computing the Voronoi diagram within the bounding box using the Euclidean distance d_{voro} , we compute a GVD on the zero-level set using the geodesic distance d_{geo} .

Computing an exact GVD on an implicit zero-level set (without an explicit mesh) is challenging, so we develop a sampling-based approximation. We first densely sample points in space and then project on iso-surface χ using their UDF values and gradients, and construct a k -nearest neighbor (KNN) graph on these samples (using $k = 20$ in our experiments). Next, we prune edges from this graph that likely do not lie on the surface. In particular, we remove any edge if either (1) the unsigned distance value at its midpoint is above a threshold (*i.e.*, $F(1/2(x_i + x_j)) > \epsilon_{\text{udf}}$), indicating the midpoint is off the surface, or (2) the UDF gradient at either endpoint is too aligned with the edge’s direction (quantified by the dot product exceeding ϵ_{grad}), indicating the edge is not tangent to the surface. After this filtering, we treat each seed as a source and run a sweeping algorithm [Xin et al. 2022] on the remaining graph to label every sample with its nearest seed in terms of geodesic distance, effectively simulating a flooding process on the surface. Finally, we construct the triangle connectivity (the dual of the approximate GVD) by examining the labeled samples: for each surface sample labeled i (nearest to seed x_i), if it has neighboring samples labeled j and k (with $j \neq i$ and $k \neq i$), we introduce a triangle connecting seeds (x_i, x_j, x_k) in the mesh. Each such triangle corresponds to a junction where three Voronoi regions meet on the surface.

3.4 Mesh Thinning

The initial mesh produced by the geodesic Voronoi diagram (GVD) reconstruction is inherently *thick*, as the dual of the GVD introduces flat but solid volumetric cells. As a result, the extracted surface is not yet a thin manifold. To eliminate these artifacts and recover a clean surface, we apply a *thinning* procedure inspired by [Wang et al. 2024, 2022, 2025].

We begin by detecting all solid tetrahedral cells embedded in the triangle mesh and iteratively prune triangle pairs from each tetrahedron without altering the overall mesh topology. Figure 9 illustrates the thinning operation on a single tetrahedron. Repeatedly removing such pairs from all detected tetrahedra collapses the flat volumes, yielding a thinner and more consistent surface mesh.

However, not all volumetric artifacts are tetrahedral; in practice, some remaining solid cells form more complex polyhedral structures. To address these cases, we iteratively remove small manifold components (defined as connected components with fewer than 10 faces in our experiments) until none remain. This post-processing step eliminates residual non-manifold polyhedral artifacts, resulting in a cleaner, more compact, and topologically valid surface mesh.

The effectiveness of our results relies on both the optimization and the thinning process. As shown in Figure 10, we conduct an

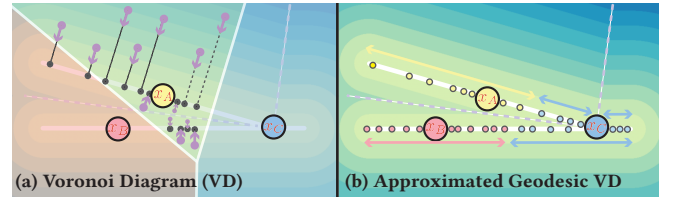


Fig. 8. Illustration of constructing an approximate geodesic Voronoi diagram (GVD) from a standard Voronoi diagram (VD). (a) Points are densely sampled in space and around the seeds, then projected onto the zero-level set. (b) The approximate GVD is computed by running a sweeping algorithm from each seed. See Sec. 3.3 for details.

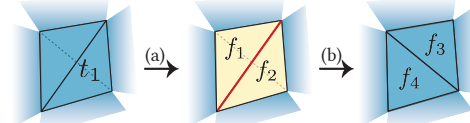


Fig. 9. Illustration of the thinning process for a flat tetrahedron t_1 in a 3D reconstructed mesh. (a) A triangle pair (f_1, f_2) sharing a manifold edge with highest UDF value on its centroid is selected for pruning. (b) After removing this pair, the remaining faces (f_3, f_4) constitute the pruned surface.



Fig. 10. We apply our thinning method described in Sec. 3.4 to both the dual-contouring-based method [Zhang et al. 2023] and our approach. The comparison illustrates that the high-quality of our results relies on both the optimization and the thinning process. Non-manifold regions are highlighted in red.

ablation study in which our thinning procedure is applied as a post-processing step to both the output of DualMeshUDF [Zhang et al. 2023] and our own method.

4 Experiments

We implemented VoroUDF in Python with C++ bindings and conducted all experiments on a MacBook Pro equipped with an Apple M3 Pro chip and 36GB of memory. All baseline methods were executed on a Linux machine with a 16-core AMD Ryzen processor and an NVIDIA RTX 3090 GPU. All 3D models in the figures are rendered using BlenderToolbox [Liu 2018]. We will release our code on GitHub publicly upon acceptance.

Optimization. The full optimization procedure is summarized in Alg. 1, with a termination threshold denoted by δ . The inner loop (line 5) terminates when either the relative change in the L-BFGS gradients falls below δ or the maximum number of iterations is reached. The outer loop (line 2) stops when the inner loop finishes without

ALGORITHM 1: Optimization

Data: Unsigned distance function $F(\mathbf{x})$ with gradients
Result: Reconstructed mesh \mathcal{M}_r

- 1 Initialize N seeds $\{\mathbf{x}_i\}_{i=1}^N$
- 2 **while** optimization not converged **do**
- 3 Update seeds using L_1 tangent energy in Sec. 3.1;
- 4 Recompute the repulsive kernel width σ ;
- 5 **while** stopping condition not satisfied **do**
- 6 Project seeds $\{\mathbf{x}_i\}$ using $F(\mathbf{x}_i)$ and its gradients;
- 7 Re-compute Voronoi diagram;
- 8 Sample each Voronoi cell of $\{\mathbf{x}_i\}_{i=1}^N$;
- 9 **for** each seed \mathbf{x}_i **do**
- 10 **for** each neighbors \mathbf{x}_j of \mathbf{x}_i **do**
- 11 | Compute E_{rep}^{ij} and \mathbf{g}^{ij} ;
- 12 | **end**
- 13 | Sum the total force $\mathbf{g}^i = \sum_j \mathbf{g}^{ij}$;
- 14 | Compute projected \mathbf{g}_{proj}^i using Eq. 6;
- 15 | **end**
- 16 | Sum the total energy E_{rep} using Eq. 5;
- 17 | Run L-BFGS with E_{rep} and $\mathbf{g}_{proj} = \sum_i \mathbf{g}_{proj}^i$;
- 18 | **end**
- 19 Project seeds $\{\mathbf{x}_i\}$ using $F(\mathbf{x}_i)$ and its gradients;
- 20 **end**
- 21 Compute reconstructed mesh in Sec. 3.3;
- 22 Apply mesh thinning in Sec. 3.4;

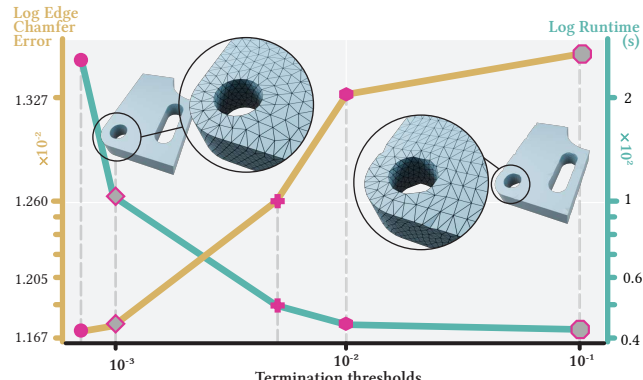


Fig. 11. Ablation study showing the effect of the termination threshold δ on runtime and reconstruction quality. Lower values of δ reduce the edge Chamfer error but incur higher computational cost. We choose $\delta = 10^{-3}$ as a practical trade-off between accuracy and efficiency.

performing any updates, indicating convergence. We present an ablation study in Figure 11 to illustrate how varying δ affects both runtime and reconstruction quality. In our experiments, we use $\delta = 10^{-3}$ as it achieves low edge Chamfer error while maintaining reasonable runtime.

Comparison Methods. We compare our method against seven baseline approaches, which fall into three main categories. The **marching-cubes-based methods** include MeshUDF [Guillard et al. 2022], CapUDF [Zhou et al. 2022], GeoUDF [Ren et al. 2023], and the learning-based method NSDUDF [Stella et al. 2024]. For MeshUDF,

CapUDF, and GeoUDF, we use the *standalone mesh extraction modules* provided in their released code. Since CapUDF’s extraction duplicates vertices per grid cell, we apply the same post-processing step used in MeshUDF to remove duplicate vertices for consistency. For NSDUDF, we evaluate the publicly released model trained on the ABC dataset across all benchmarks. We also compare against two **double-covering-based methods**, DCUDF [Hou et al. 2023] and DCUDF2 [Chen et al. 2025], and one **dual-contouring-based method**, DualMeshUDF [Zhang et al. 2023]. All methods are evaluated under comparable reconstruction settings, with a similar number of vertices ($\#v$) in the output mesh. Additional comparisons at higher resolutions are included in the Supplementary Material.

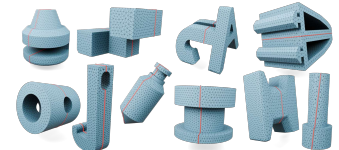
Evaluation Metrics. To evaluate the quality of the reconstructed meshes, we adopt several standard metrics. For mesh regularity, we report *Triangle Quality* (TQ) [Frey and Borouchaki 1999] and *Topology Error* (TD). To assess geometric fidelity between the reconstructed surface and the ground truth, we use the L_1 *Chamfer Error* (CD) and the *Hausdorff Error* (HD). To evaluate sharp feature reconstruction, we report the L_1 *Edge Chamfer Error* (ECD) [Chen and Zhang 2021]. For non-manifold regions, we introduce the *Non-Manifold Chamfer Error* ($NM\text{-}CD$) to measure reconstruction accuracy. Due to space constraints, detailed definitions of TQ , $L_1\text{-}CD$, $L_1\text{-}ECD$, and HD are provided in the Supplementary Material.

Topology Error (TD). We use the *Euler characteristic* as a measure of mesh topology and report the absolute difference between the Euler characteristic of the source UDF isosurface and that of the reconstructed mesh. This metric reflects the topological discrepancy between the reconstruction and the ground truth.

Non-Manifold Chamfer Error (NM-CD). We detect non-manifold edges (shared by more than two faces) and non-manifold vertices in both the source and reconstructed meshes. We then densely sample points on these regions and compute the bidirectional Chamfer distance between the two sets of samples. The L_1 error of this distance is reported as the $NM\text{-}CD$ metric, quantifying the geometric accuracy of reconstructed non-manifold structures.

4.1 Comparisons on Non-Manifold Models

To quantitatively evaluate our method on non-manifold geometry, we construct a set of 10 synthetic non-manifold models (see inset of our results). Each model is generated by selecting a mesh from the ABC dataset [Koch et al. 2019], cutting it with a plane, and then merging the two cut parts with a narrow overlapping band (see Figure 12, source). We densely sample points on each of the two cut meshes and identify those near the opposing part, which we highlight in red in Figure 12. These red samples approximate the ground-truth non-manifold edges in the merged mesh. Quantitative results are reported in Table 4, and corresponding qualitative comparisons are shown in Table 4. We select one representative method from each category to compare in the figure. More results are provided in the Supplementary Material. Among all methods evaluated, ours is



the only one that faithfully reconstructs non-manifold structures. It is worth noting that the double-covering-based methods [Chen et al. 2025; Hou et al. 2023] completely fail to recover non-manifold structures, as they produce double-layered meshes by design, resulting in their metric $NM\text{-}CD = \text{Inf}$.

Table 1. Quantitative comparison on 10 synthetic models with non-manifold edges against seven state-of-the-art methods, using a similar number of vertices ($\#v$) in the reconstructed meshes. The **best** scores are shown in bold, and the second best scores are underlined.

Method	#v	CD $\times 10^3 \downarrow$	HD $\times 10^3 \downarrow$	ECD $\times 10^2 \downarrow$	TQ \uparrow	TD \downarrow	NM-CD $\times 10^3 \downarrow$
MeshUDF	7.5k	64.09	33.07	32.36	0.65	157.2	1017.12
CapUDF	6.3k	53.25	126.86	25.91	0.57	261.3	<u>Inf</u>
GeoUDF	4.5k	22.43	36.61	37.28	0.65	142.1	1499.15
NSDUDF	<u>3.6k</u>	20.29	22.08	99.55	0.64	84.7	<u>267.09</u>
DCUDF	8.2k	80.96	32.27	100.29	0.71	45.1	<u>Inf</u>
DCUDF2	9.1k	64.76	28.13	110.31	0.72	<u>45.0</u>	<u>Inf</u>
DualMeshUDF	5k	17.89	11.35	<u>4.92</u>	0.52	744.3	375.24
Ours	2.9k	17.04	6.74	4.05	0.84	43.6	14.35

4.2 Comparisons on CAD models

We present quantitative comparison results on 100 CAD models taken from Xu et al. [2024] in Tab. 2, and corresponding qualitative comparisons in Figure 14. Our method consistently outperforms all baselines across nearly all metrics, while maintaining a comparable number of vertices in the reconstructed mesh. Additional results using denser resolutions for the seven baseline methods are provided in the Supplementary Material.

Table 2. Quantitative comparison on the 100 ABC models [Xu et al. 2024] against seven state-of-the-art methods, using a similar number of vertices ($\#v$) in the reconstructed meshes. The **best** scores are shown in bold, and the second best scores are underlined.

Method	#v	CD $\times 10^3 \downarrow$	HD $\times 10^3 \downarrow$	ECD $\times 10^2 \downarrow$	TQ \uparrow	TD \downarrow
MeshUDF	4.2k	58.80	28.39	42.78	0.65	47.16
CapUDF	6.7k	44.10	94.71	29.36	0.52	189.64
GeoUDF	2.6k	19.59	31.58	52.33	<u>0.67</u>	59.07
NSDUDF	<u>2.3k</u>	<u>17.17</u>	15.78	103.82	0.65	13.5
DCUDF	4.8k	91.12	51.34	123.44	0.62	<u>1.17</u>
DCUDF2	3.8k	109.57	53.51	130.63	0.65	1.44
DualMeshUDF	3.1k	30.62	<u>10.60</u>	<u>4.98</u>	0.52	694.74
Ours	2.2k	13.07	5.85	2.38	0.83	0.28

4.3 Comparisons on Garment Models

We further evaluate our method against seven state-of-the-art baselines on 100 garment models from the DeepFashion3D dataset [Zhu et al. 2020]. Quantitative results are reported in Tab. 3, and qualitative comparisons are shown in Figure 14. Our method would introduce non-manifold edges (highlighted in red) in regions under the armpit, where two layers of the surface nearly coincide. This contributes to a slightly higher topology error (TD) compared to double-covering-based methods [Chen et al. 2025; Hou et al. 2023], which avoid such configurations by design.

Table 3. Quantitative comparison on the top 100 DeepFashion3D [Zhu et al. 2020] models against seven state-of-the-art methods, using a similar number of vertices ($\#v$) in the reconstructed meshes. The **best** scores are shown in bold, and the second best scores are underlined.

Method	#v	CD $\times 10^3 \downarrow$	HD $\times 10^3 \downarrow$	TQ \uparrow	TD \downarrow
MeshUDF	3.9k	64.7	31.3	0.61	75.68
CapUDF	5.2k	<u>27.39</u>	<u>30.90</u>	0.53	<u>322.11</u>
GeoUDF	2.6k	16.79	31.77	0.61	76.13
DCUDF	3.8k	107.36	78.15	0.70	<u>1.23</u>
DCUDF2	4.1k	89.86	68.85	<u>0.71</u>	1.18
DualMeshUDF	3k	<u>14.17</u>	<u>27.01</u>	0.52	499.48
Ours	2.6k	13.09	20.65	0.74	1.76

5 Limitations & Conclusion

We have introduced VoroUDF, a surface reconstruction algorithm that generates high-quality triangle meshes from unsigned distance fields. Unlike all prior work on this task, our results preserve faithful non-manifold structures, sharp features, and open surfaces. Our method leverages a Voronoi-based partitioning framework, combined with an L_1 tangent energy and a feature-aware repulsive energy, to achieve state-of-the-art performance across a wide range of input scenarios.

Our Voronoi-based spatial partitioning eliminates the need for subdividing voxel grids and is better suited for preserving thin structures. However, it requires seed points to be initialized near such features; without adequate initialization, small-scale geometry may be missed or poorly reconstructed. In our current implementation, seeds are uniformly sampled across the domain, which leaves coverage to chance in complex regions. In future work, we plan to explore adaptive or data-driven seed initialization strategies to ensure sufficient sampling around thin or intricate structures.

Our method demonstrates strong empirical performance in preserving complex topologies such as non-manifold structures, it unfortunately lacks a formal theoretical guarantee of topological correctness. In some cases, our reconstruction may introduce very small amount of non-manifold edges (comparing to dual-counting-based method [Zhang et al. 2023]) even when the input source is a true manifold (see inset). This behavior is most evident in regions where surface layers nearly coincide, such as the armpit area in garment models. Additionally, some triangles near open boundaries may be erroneously removed due to over-thinning. As future work, we plan to incorporate topological validation or correction mechanisms to improve robustness in these challenging cases.

Our L_1 tangent energy and repulsive energy formulations are designed to operate reliably on clean UDFs with accurate gradients. However, the effect of input noise, either in the distance values or gradients, has not been systematically studied. Investigating the



robustness of our method under noisy conditions and exploring denoising techniques or regularization strategies will be an important direction for future research.

Our work focuses on reconstructing UDFs with complex geometries and topologies. With it, we aim to contribute to a growing body of research that helps bridge the gap between the flexible modeling practices of 3D artists and the geometric quality and fidelity requirements of downstream applications. We also seek to help connect the 3D generative deep learning and geometry processing communities, enabling generated shapes to be used in real-world tasks like rendering, physical simulation, and animation.

Acknowledgments

The Geometry and the City lab at Columbia University is supported by generous gifts from nTop, Adobe and Braid Technologies.

References

Alan Brunton and Lubna Abu Rmaileh. 2021. Displaced signed distance fields for additive manufacturing. *ACM Transactions on Graphics (TOG)* 40, 4 (2021), 1–13.

Xuhui Chen, Fugang Yu, Fei Hou, Wencheng Wang, Zhebin Zhang, and Ying He. 2025. DCUDF2: Improving efficiency and accuracy in extracting zero level sets from unsigned distance fields. *IEEE Transactions on Visualization and Computer Graphics* (2025).

Zhiqin Chen, Andrea Tagliasacchi, Thomas Funkhouser, and Hao Zhang. 2022. Neural dual contouring. *ACM Transactions on Graphics (TOG)* 41, 4 (2022), 1–13.

Zhiqin Chen and Hao Zhang. 2021. Neural marching cubes. *ACM Transactions on Graphics (TOG)* 40, 6 (2021), 1–15.

Julian Chibane, Gerard Pons-Moll, et al. 2020. Neural unsigned distance fields for implicit function learning. *Advances in Neural Information Processing Systems* 33 (2020), 21638–21652.

Pascal J Frey and Houman Borouchaki. 1999. Surface mesh quality evaluation. *International journal for numerical methods in engineering* 45, 1 (1999), 101–118.

Benoit Guillard, Federico Stella, and Pascal Fua. 2022. Meshudf: Fast and differentiable meshing of unsigned distance field networks. In *European conference on computer vision*. Springer, 576–592.

Fei Hou, Xuhui Chen, Wencheng Wang, Hong Qin, and Ying He. 2023. Robust zero level-set extraction from unsigned distance fields based on double covering. *ACM Transactions on Graphics (TOG)* 42, 6 (2023), 1–15.

Ge Jin, Younhyun Jung, Lei Bi, and Jinman Kim. 2024. MISNeR: Medical Implicit Shape Neural Representation for Image Volume Visualisation. In *Computer Graphics Forum*, Vol. 43. Wiley Online Library, e15222.

Tao Ju, Franck Losasso, Scott Schaefer, and Joe Warren. 2002. Dual contouring of hermite data. In *Proceedings of the 29th annual conference on Computer graphics and interactive techniques*. 339–346.

Sebastian Koch, Albert Matveev, Zhongshi Jiang, Francis Williams, Alexey Artemov, Evgeny Burnaev, Marc Alexa, Denis Zorin, and Daniele Panozzo. 2019. Abc: A big cad model dataset for geometric deep learning. In *Proceedings of the IEEE/CVF conference on computer vision and pattern recognition*. 9601–9611.

Hsueh-Ti Derek Liu. 2018. *Blender Toolbox*. <https://github.com/HTDerekLiu/BlenderToolbox>

Yu-Tao Liu, Li Wang, Jie Yang, Weikai Chen, Xiaoxu Meng, Bo Yang, and Lin Gao. 2023. Neudf: Leaning neural unsigned distance fields with volume rendering. In *Proceedings of the IEEE/CVF conference on computer vision and pattern recognition*. 237–247.

Xiaoxiao Long, Cheng Lin, Lingjie Liu, Yuan Liu, Peng Wang, Christian Theobalt, Taku Komura, and Wenping Wang. 2023. Neuraludf: Learning unsigned distance fields for multi-view reconstruction of surfaces with arbitrary topologies. In *Proceedings of the IEEE/CVF conference on computer vision and pattern recognition*. 20834–20843.

William E. Lorensen and Harvey E. Cline. 1987. Marching cubes: A high resolution 3D surface construction algorithm. *SIGGRAPH Comput. Graph.* 21, 4 (Aug. 1987), 163–169. doi:10.1145/37402.37422

Siyu Ren, Junhui Hou, Xiaodong Chen, Ying He, and Wenping Wang. 2023. Geoudf: Surface reconstruction from 3d point clouds via geometry-guided distance representation. In *Proceedings of the IEEE/CVF International Conference on Computer Vision*. 14214–14224.

Scott Schaefer and Joe Warren. 2002. Dual contouring: The secret sauce. *Technical Report* 2, 408 (2002).

Kristine Sørensen, Oscar Camara, Ole De Backer, Klaus F Kofoed, and Rasmus R Paulsen. 2022. NUDF: neural unsigned distance fields for high resolution 3D medical image segmentation. In *2022 IEEE 19th International Symposium on Biomedical Imaging (ISBI)*. IEEE, 1–5.

Federico Stella, Nicolas Talabot, Hieu Le, and Pascal Fua. 2024. Neural surface detection for unsigned distance fields. In *European Conference on Computer Vision*. Springer, 394–409.

Ningna Wang, Hui Huang, Shibo Song, Bin Wang, Wenping Wang, and Xiaohu Guo. 2024. MATTopo: Topology-preserving Medial Axis Transform with Restricted Power Diagram. *ACM Transactions on Graphics (TOG)* 43, 4 (2024). doi:10.1145/3687763

Ningna Wang, Bin Wang, Wenping Wang, and Xiaohu Guo. 2022. Computing Medial Axis Transform with Feature Preservation via Restricted Power Diagram. *ACM Transactions on Graphics (Proceedings of SIGGRAPH Asia 2022)* 41, 6 (2022).

Ningna Wang, Rui Xu, Yibo Yin, Zichun Zhong, Taku Komura, Wenping Wang, and Xiaohu Guo. 2025. MATStruct: High-quality Medial Mesh Computation via Structure-aware Variational Optimization. In *Proceedings of the SIGGRAPH Asia 2025 Conference Papers*. 1–12.

Andrew P Witkin and Paul S Heckbert. 1994. Using particles to sample and control implicit surfaces. In *Proceedings of the 21st annual conference on Computer graphics and interactive techniques*. 269–277.

Shiqing Xin, Pengfei Wang, Rui Xu, Dongming Yan, Shuangmin Chen, Wenping Wang, Caiming Zhang, and Changhe Tu. 2022. SurfaceVoronoi: Efficiently computing voronoi diagrams over mesh surfaces with arbitrary distance solvers. *ACM Transactions on Graphics (TOG)* 41, 6 (2022), 1–12.

Cheng Xu, Fei Hou, Wencheng Wang, Hong Qin, Zhebin Zhang, and Ying He. 2025. Details enhancement in unsigned distance field learning for high-fidelity 3d surface reconstruction. In *Proceedings of the AAAI Conference on Artificial Intelligence*, Vol. 39. 8806–8814.

Rui Xu, Longdu Liu, Ningna Wang, Shuangmin Chen, Shiqing Xin, Xiaohu Guo, Zichun Zhong, Taku Komura, Wenping Wang, and Changhe Tu. 2024. CWF: consolidating weak features in high-quality mesh simplification. *ACM Transactions on Graphics (TOG)* 43, 4 (2024), 1–14.

Congyi Zhang, Guying Lin, Lei Yang, Xin Li, Taku Komura, Scott Schaefer, John Keyser, and Wenping Wang. 2023. Surface extraction from neural unsigned distance fields. In *Proceedings of the IEEE/CVF International Conference on Computer Vision*. 22531–22540.

Luotao Zhang, Chunqing Ran, Xiaobo Zhang, Hao Yu, Shuo Han, and Yilan Chen. 2026. MB-UDF: A self-supervised model for continuous representation of seafloor topography using multibeam echo sounder data. *International Journal of Applied Earth Observation and Geoinformation* 146 (2026), 105056.

Fang Zhao, Wenhao Wang, Shengcai Liao, and Ling Shao. 2021. Learning anchored unsigned distance functions with gradient direction alignment for single-view garment reconstruction. In *Proceedings of the IEEE/CVF International Conference on Computer Vision*. 12674–12683.

Zichun Zhong, Xiaohu Guo, Wenping Wang, Bruno Lévy, Feng Sun, Yang Liu, Weihua Mao, et al. 2013. Particle-based anisotropic surface meshing. *ACM Trans. Graph.* 32, 4 (2013), 99–1.

Junsheng Zhou, Baorui Ma, Yu-Shen Liu, Yi Fang, and Zhizhong Han. 2022. Learning consistency-aware unsigned distance functions progressively from raw point clouds. *Advances in Neural Information Processing Systems* 35 (2022), 16481–16494.

Heming Zhu, Yu Cao, Hang Jin, Weikai Chen, Dong Du, Zhangye Wang, Shuguang Cui, and Xiaoguang Han. 2020. Deep fashion3d: A dataset and benchmark for 3d garment reconstruction from single images. In *European Conference on Computer Vision*. Springer, 512–530.

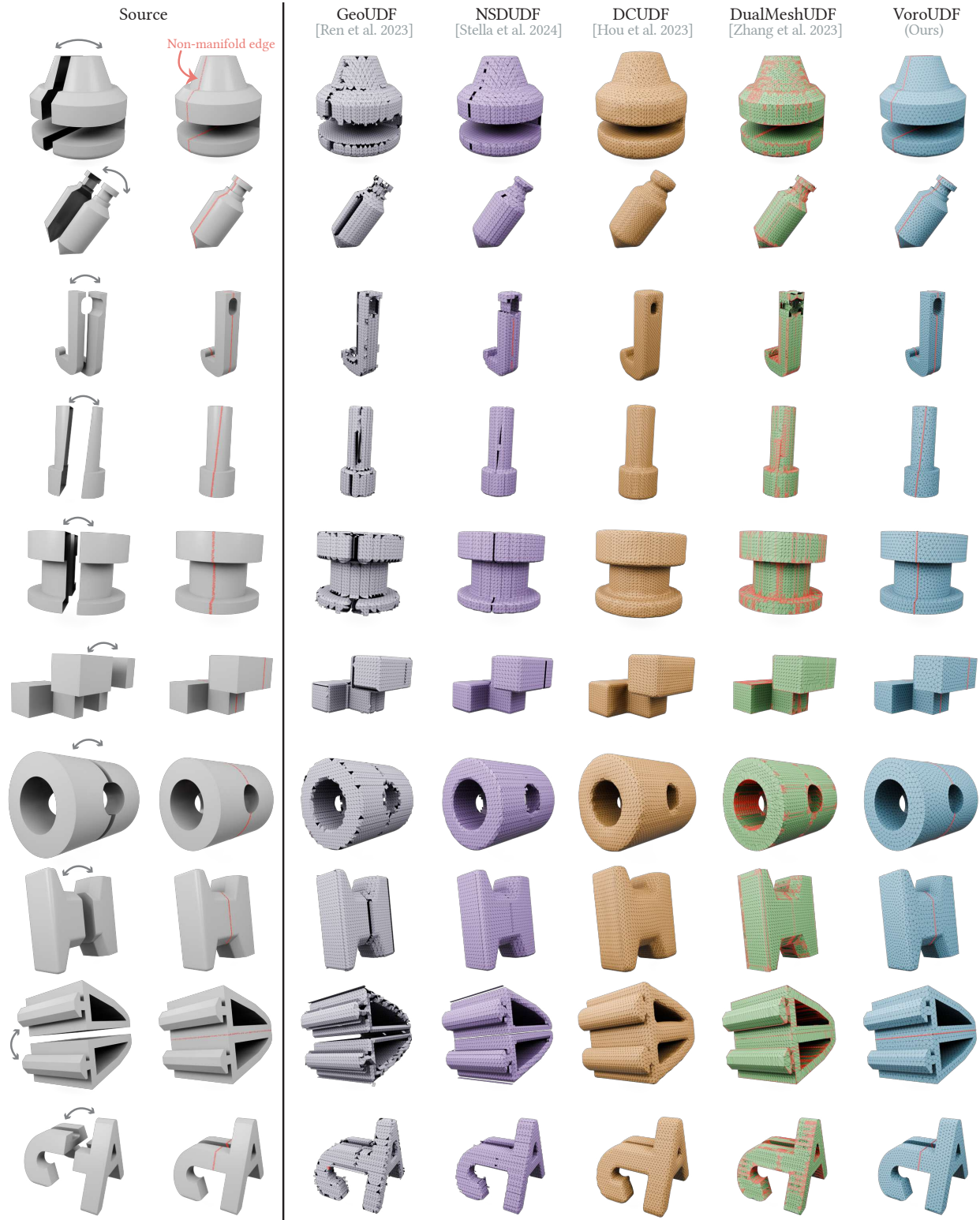


Fig. 12. Qualitative comparison with 4 state-of-the-art methods on 10 synthetic non-manifold shapes, each using a similar number of vertices in the reconstructed mesh. We select one representative method from each category: GeoUDF [Ren et al. 2023] (marching-cubes-based), NSDUDF [Stella et al. 2024] (learning-based), DCUDF [Hou et al. 2023] (double-covering-based), and DualMeshUDF [Zhang et al. 2023] (dual-contouring-based). Non-manifold regions are highlighted in red.

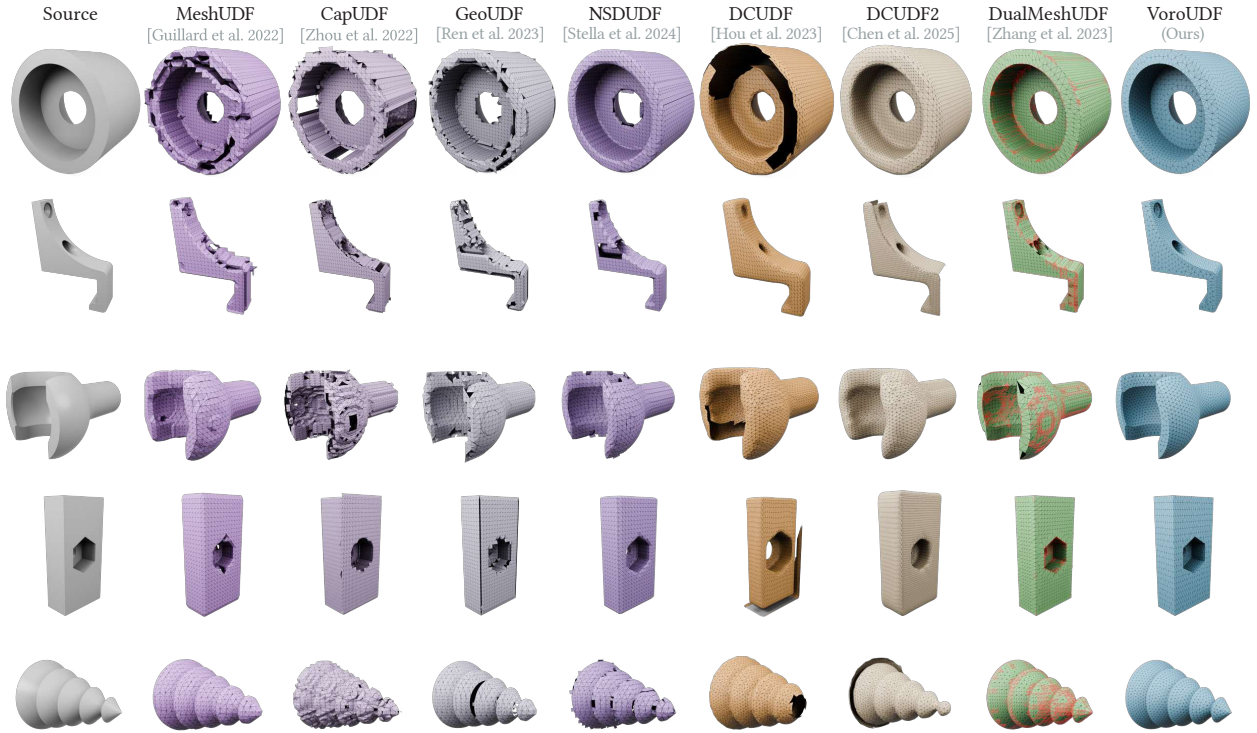


Fig. 13. Comparison with 7 state-of-the-art methods with similar number of vertices in the final reconstructed mesh on the ABC dataset. Non-manifold structures are highlighted in red.

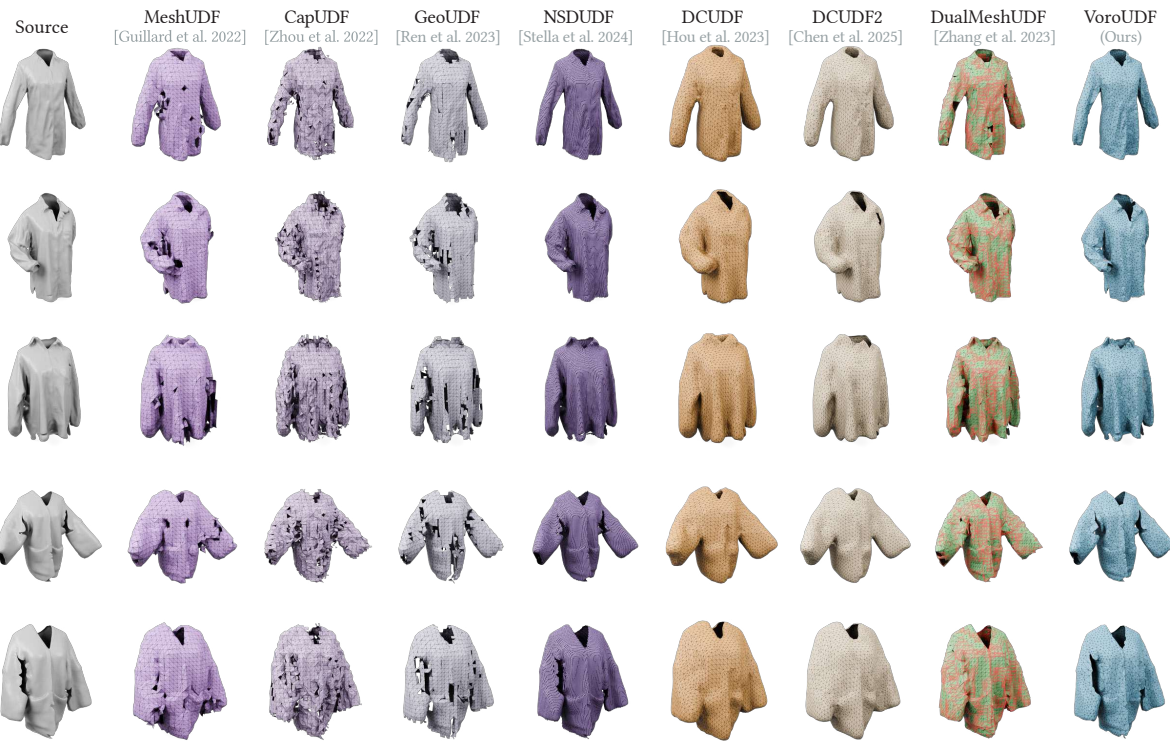


Fig. 14. Comparison with 7 state-of-the-art methods with similar number of vertices in the final reconstructed mesh on the DeepFashion3D dataset. Non-manifold structures are highlighted in red.

A Supplementary Material

B Evaluation Metrics

Triangle Quality (TQ). To evaluate triangle quality, we use the TQ indicator [Frey and Borouchaki 1999], where a value closer to 1.0 indicates a triangle that is nearly equilateral. We use the following equation to evaluate the triangle quality,

$$TQ(t) = \frac{6}{\sqrt{3}} \cdot \frac{S_t}{p_t \cdot h_t} \quad (7)$$

where S_t , p_t , and h_t denote the area, half-perimeter, and the longest edge length of the triangle t , respectively.

L_1 Chamfer Error (CD). The Chamfer error measures the overall geometric discrepancy between the reconstructed surface mesh and the ground truth shape. In our experiments, we report the L_1 version of this metric to evaluate reconstruction accuracy.

L_1 Edge Chamfer Error (ECD). To assess the accuracy of sharp feature reconstruction, we adopt the *edge* Chamfer distance introduced by Chen and Zhang [2021], computed using the L_1 norm.

Hausdorff Error (HD). To measure the difference between the reconstructed mesh and the source, we use the Hausdorff Error as the indicator. Here, HD^1 is the one-sided Hausdorff distance from the original surface to the surface reconstructed from MAT, and HD^2 is the distance in reverse side. All Hausdorff distances are evaluated as percentages of the distance over the diagonal lengths of the models' bounding box. The HD is the maximum of HD^1 and HD^2 . The Hausdorff distance can reveal if there is anything missing or redundant in the reconstructed geometry (e.g., a hole or a floating piece).

B.1 More Comparisons on Non-Manifold Models

We compare our method against seven state-of-the-art baselines on 10 synthetic models containing non-manifold edges, evaluated at higher resolution (2^7). Quantitative results are reported in Table 4, and qualitative comparisons are shown in Figure 15.

Table 4. Quantitative comparison on 10 synthetic models with non-manifold edges, evaluated against seven state-of-the-art methods with higher resolution (2^7). The **best** scores are shown in bold, and the second best scores are underlined.

Method	#v	CD x10 ³ ↓	HD x10 ³ ↓	ECD x10 ² ↓	TQ ↑	TD ↓	NM-CD x10 ³ ↓
MeshUDF	121k	23.64	7.50	31.47	0.66	479.7	1267.02
CapUDF	103k	18.56	9.30	20.96	0.58	1531.7	Inf
GeoUDF	71k	17.12	8.55	32.52	0.67	521.9	843.62
NSDUDF	60k	17.02	<u>4.06</u>	58.08	0.64	257.3	784.42
DCUDF	159k	27.41	6.78	124.62	0.71	45.5	Inf
DCUDF2	175k	21.72	5.80	120.64	<u>0.72</u>	45.4	Inf
DualMeshUDF	8.4k	17.21	<u>1.35</u>	<u>3.78</u>	0.61	22k	418.01
Ours	2.9k	<u>17.04</u>	6.74	<u>4.05</u>	<u>0.84</u>	43.6	<u>14.35</u>

B.2 More Comparisons on CAD models

We compare our method against seven state-of-the-art baselines on 100 CAD models [Xu et al. 2024], evaluated at higher resolution (2^7). Quantitative results are presented in Table 5, and qualitative comparisons are shown in Figure 16 and Figure 17.

Table 5. Quantitative comparison on 100 ABC models [Xu et al. 2024], evaluated against seven state-of-the-art methods with higher resolution (2^7). The **best** scores are shown in bold, and the second best scores are underlined.

Method	#v	CD x10 ³ ↓	HD x10 ³ ↓	ECD x10 ² ↓	TQ ↑	TD ↓
MeshUDF	70k	33.5	6.3	43.35	0.67	239.15
CapUDF	111k	14.90	6.16	18.42	0.53	813.06
GeoUDF	42k	13.13	6.59	38.59	<u>0.68</u>	296.63
NSDUDF	36k	13.04	<u>2.79</u>	62.83	0.66	94.02
DCUDF	67k	41.24	12.32	137.10	0.64	<u>0.32</u>
DCUDF2	95k	20.69	7.98	96.81	0.60	0.35
DualMeshUDF	48k	29.19	0.98	<u>2.83</u>	0.61	10053.07
Ours	2.2k	<u>13.07</u>	5.85	<u>2.38</u>	<u>0.83</u>	0.28

B.3 More Comparisons on garment models

We further compare our method with seven state-of-the-art methods on (first) 100 garment shapes from DeepFashion3D [Zhu et al. 2020] dataset. The results from seven state-of-the-art methods are generated at higher resolution (2^7), shown in Table 6, Figure 18 and Figure 19.

Table 6. Quantitative comparison on first 100 DeepFashion3D models [Zhu et al. 2020], evaluated against seven state-of-the-art methods with higher resolution (2^7). The **best** scores are shown in bold, and the second best scores are underlined.

Method	#v	CD x10 ³ ↓	HD x10 ³ ↓	TQ ↑	TD ↓
MeshUDF	67k	20.53	<u>8.20</u>	0.61	726.00
CapUDF	77k	13.36	9.05	0.53	2055.21
GeoUDF	37k	11.95	10.07	0.62	237.34
DCUDF	53k	29.36	37.39	<u>0.72</u>	4.43
DCUDF2	58k	20.04	35.73	0.71	<u>3.33</u>
DualMeshUDF	51k	<u>12.08</u>	7.62	0.58	8131.65
Ours	2.6k	13.09	20.65	<u>0.74</u>	1.76

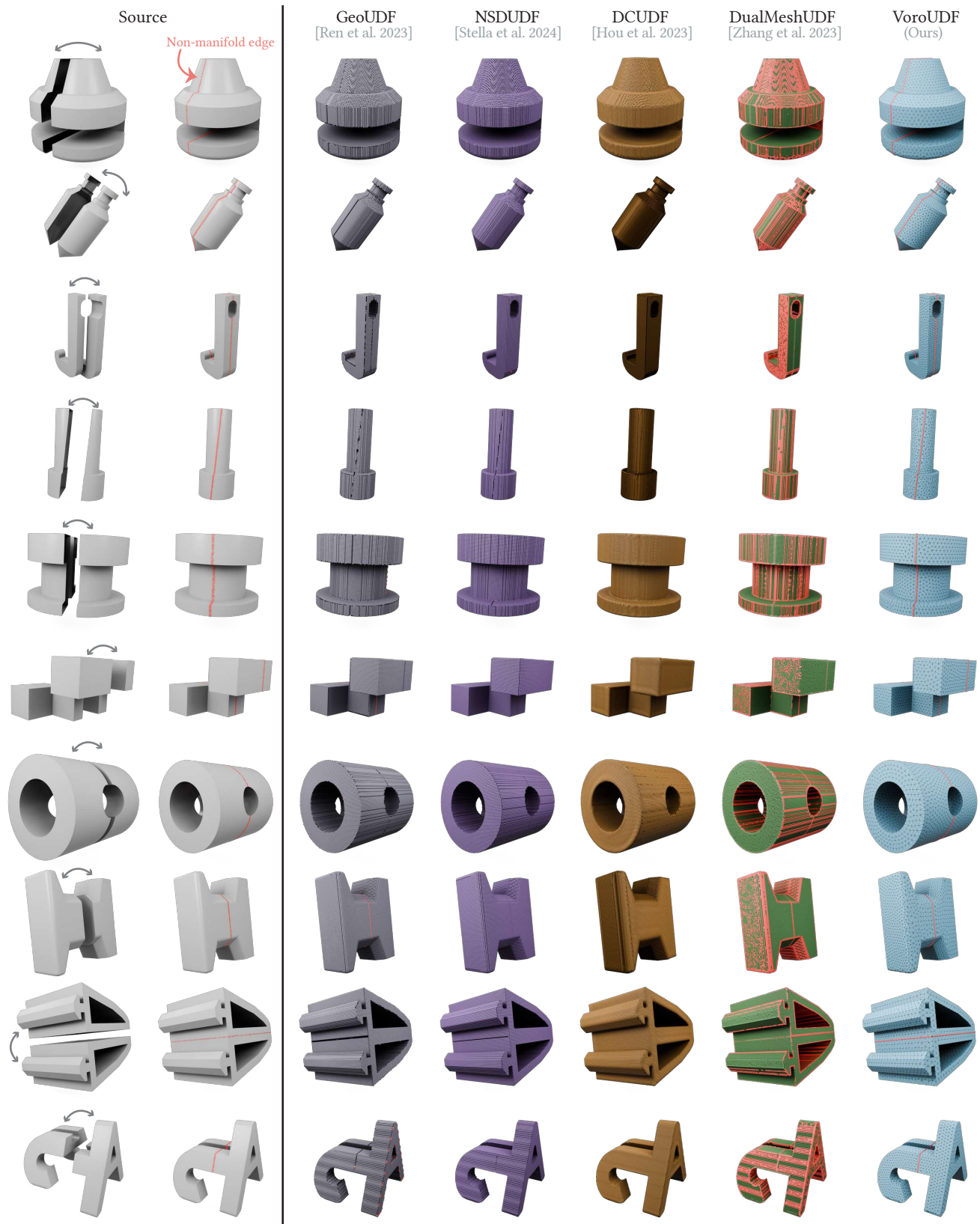
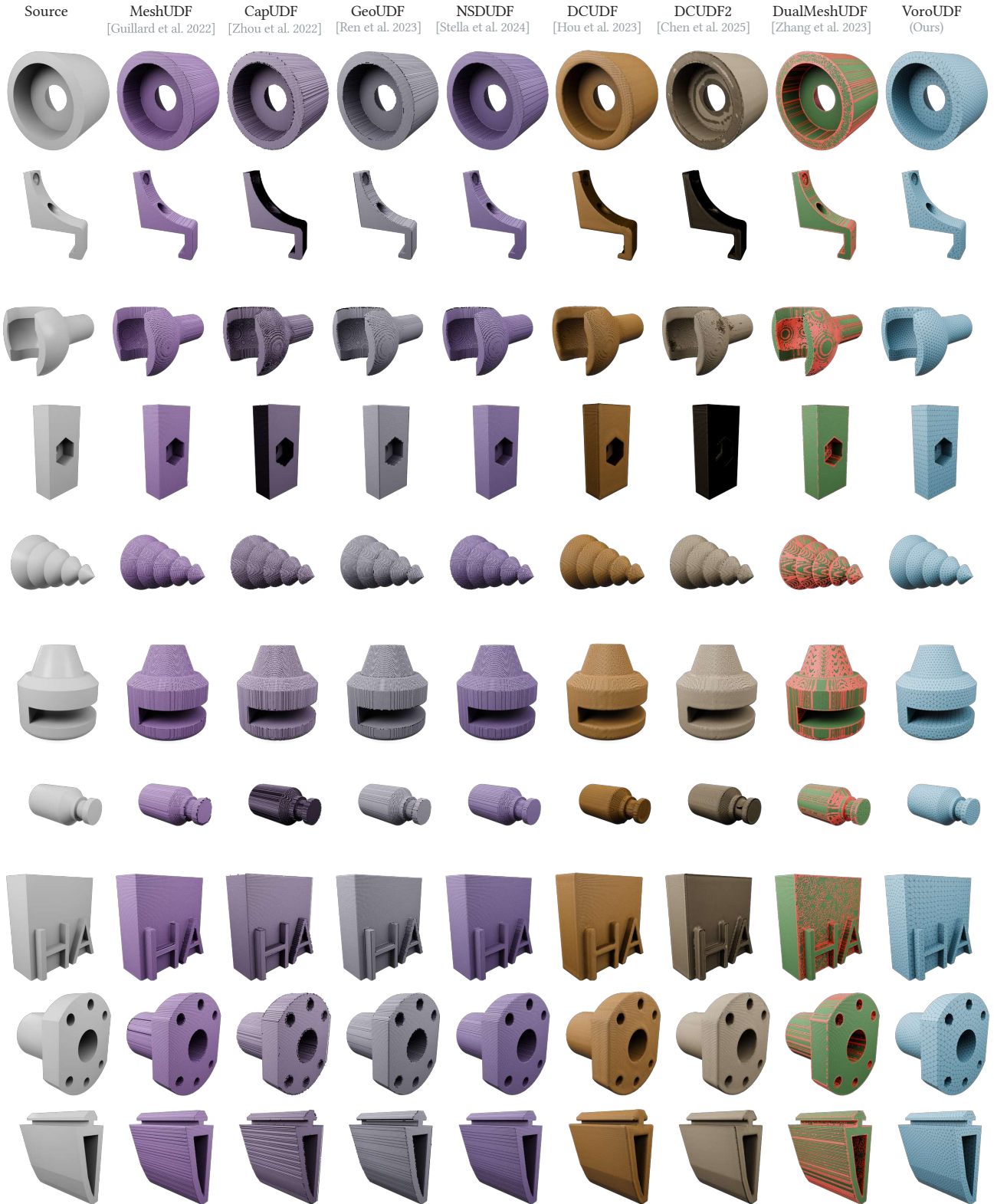


Fig. 15. Qualitative comparison on 10 synthetic models with non-manifold edges, evaluated against seven state-of-the-art methods at higher resolution (2^7). Non-manifold edges are highlighted in red.



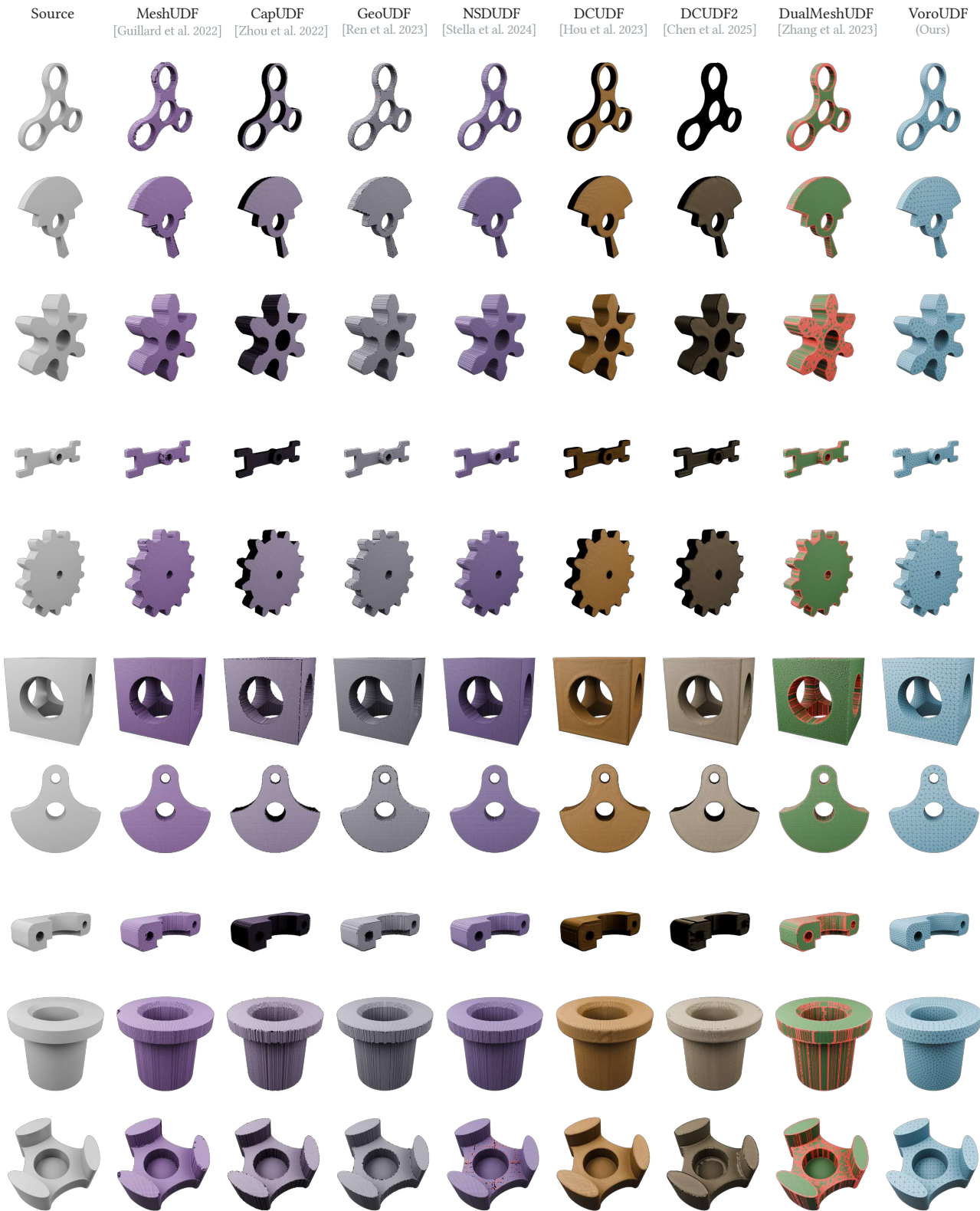


Fig. 17. Qualitative comparison on 100 ABC models (part 2), evaluated against seven state-of-the-art methods at higher resolution (2^7). Non-manifold edges are highlighted in red.



